

SPECTRAL PROPERTIES OF THREE-DIMENSIONAL MAGNETO-HYDRODYNAMICAL ACCRETION FLOWS

K. OHSUGA^{1,2}, Y. KATO², AND S. MINESHIGE²

Draft version October 28, 2019

ABSTRACT

In spite of a large number of global three-dimensional (3D) magneto-hydrodynamical (MHD) simulations of accretion flows and jets being made recently, their astrophysical relevance for realistic situations is not well known. In order to examine to what extent the simulated MHD flows can account for the observed spectral energy distribution (SED) of Sagittarius A* (Sgr A*), for the first time we calculate the emergent spectra from 3D MHD flows in a wide range of wavelengths (from radio to X-ray) by solving the 3D radiative transfer equations. We use the simulation data by Kato, Mineshige, & Shibata (2004) and perform Monte Carlo radiative transfer simulations, in which synchrotron emission/absorption, free-free emission/absorption, and Compton/inverse Compton scattering are taken into account. We assume two temperature plasmas and calculate electron temperatures by solving the electron energy equation. Only thermal electrons are considered.

It is found that the 3D MHD flow generally over-produces X-rays by means of bremsstrahlung radiation from the regions at large radii. A flatter density profile, $\rho \propto r^{-a}$ with $a < 1$, than that of the advection-dominated accretion flow (ADAF), $\rho \propto r^{-3/2}$, is the main reason for this. If we restrict the size of the emission region to be as small as $\sim 10 r_s$, where r_s is the Schwarzschild radius, the MHD model can reproduce the basic features of the observed SED of Sgr A* during its flaring state. Yet, the spectrum in the quiescent state remains to be understood. We discuss how to resolve this issue in the context of MHD flow models. Possibilities include modifications of the MHD flow structure either by the inclusion of radiative cooling and/or significant contributions by nonthermal electrons. It is also possible that the present spectral results may be influenced by particular initial conditions. We also calculate the time-dependent spectral changes, finding that the fluxes fluctuate in a wide range of the frequency and the flux at each wavelength does not always vary coherently.

Subject headings: accretion: accretion disks — black hole physics — radiative transfer — Galaxy: center

1. INTRODUCTION

There is a long research history in the theoretical modeling of black-hole accretion flows. The standard-disk picture was first established by Shakura & Sunyaev (1973) after many attempts. In this model the gravitational energy is efficiently converted to radiation energy and is finally radiated away. Then, the disk was predicted to be luminous and relatively cold, exhibiting multi-color blackbody spectra (Mitsuda et al. 1984). The standard-disk model is widely accepted as a model for disks with moderately high accretion rates, $\dot{M} \lesssim L_E/c^2$ with L_E being the Eddington luminosity and c being the light velocity (Esin, McClintock, & Narayan 1997). In fact, the calculated spectra based on the standard disk model fits well with the thermal component of the high-state of the black hole candidates (BHCs, Ebisawa 1999), including the specific temperature gradient (Mineshige et al. 1994), and probably the big blue bump of the active galactic nuclei (AGNs, Shields 1978; Malkan 1983).

On the other hand, when the mass-accretion rate is much less than the critical value of $\sim L_E/c^2$, the radiation loss is inefficient and thus the accretion flow becomes a radiatively inefficient accretion flow (RIAF). In such a situation, the thermal energy of the gas can be advected

inward towards the black hole without much being radiated away. This basic idea, now known as the notion of advection-dominated accretion flow (ADAF), was first presented by Ichimaru (1977) and has been investigated in quite a lot of detail since the 1990's (Narayan & Yi 1994, 1995a, b; Abramowicz et al. 1995; for reviews, see Narayan, Mahadevan, & Quataert 1998; Kato, Fukue, & Mineshige 1998). Since the ADAF can reproduce hard, power-law spectra in the X-ray range, as has been observed, this model was thought to be a good representation of disks in low-luminosity AGNs (LLAGNs) and in the BHCs during their low-hard state. Remarkably, the ADAF model can nicely fit the emergent spectrum of Sagittarius A* (Sgr A*) and other black-hole objects (Narayan, Yi, & Mahadevan 1995; Manmoto, Mineshige, & Kusunose 1997; Narayan et al. 1998; Manmoto 2000; Özel, Psaltis, & Narayan 2000; Oka & Manmoto 2003). (We should keep in mind, however, that most of observational data of Sgr A* only gives upper limits except at radio and X-ray wavelengths.)

We should be aware that there are a number of serious problems inherent to the ADAF formulation. For example, the ADAF model cannot properly treat three-dimensional motion, because the ADAF model is a one-dimensional model (in the sense that only the radial structure is solved), although both of the simple arguments and hydrodynamical simulations have shown that the occurrence of convections and/or outflow seems to be a natural consequence in the RIAF (Narayan & Yi

¹ Department of Physics, Rikkyo University, Toshimaku, Tokyo 171-8501, Japan

² Yukawa Institute for Theoretical Physics, Kyoto University, Kyoto 606-8502, Japan

1994; Igumenshchev & Abramowicz 2000). The magnetic fields are treated as a single parameter, the plasma- β , to predict synchrotron emissivity, which is too simple and problematic to describe the dynamics of magnetic fields (see a comprehensive discussion in Narayan 2002). Yuan, Quataert, & Narayan (2003) recently succeeded in reproducing the spectrum of Sgr A* by introducing nonthermal electron components, but they still treat the magnetic fields in a simplified way. Recent MHD simulations have commonly shown the important role of the magnetic fields in the flow dynamics. The MHD flow is intrinsically time varying and exhibits fractal structure (e.g., Kawaguchi et al. 2000; Machida & Matsumoto 2003, hereafter referred to as MM03). To summarize, the lack of three-dimensional (3D) motion and the over-simplified treatment of magnetic fields lead to self-inconsistencies in the ADAF solution.

The global 3D MHD simulations of RIAFs were first made by Matsumoto (1999), and have been extensively performed recently by several groups (see Mineshige & Makishima 2004 for a compilation of recent works). It has been revealed by the 3D MHD simulations that the flow pattern is considerably complicated and differs significantly from that of the ADAF model (Hawley 2000; Machida, Hayashi, & Matsumoto 2000; Hawley & Krolik 2001; Machida, Matsumoto & Mineshige 2001, hereafter referred to as MMM01; Hawley & Balbus 2002, hereafter HB02; MM03; Igumenshchev, Narayan, & Abramowicz 2003, hereafter INA03). Stone & Pringle (2001, hereafter SP01) established that a complex flow pattern is produced due to a magneto-rotational instability (MRI, see also Hawley, Balbus, & Stone 2001; Hawley 2001; Balbus 2003 for a review). Since the dynamics of magnetic fields is fully solved, the 3D MHD models seem to be more suitable for describing the RIAF than other models without appropriate treatment of magnetic fields. Thus, the MHD models are expected to fit the observations. Surprisingly, however, such a critical test has not been well investigated. Some papers discussing the observational appearance of the simulated MHD flow, HB02 for example, have shown the distribution of the synchrotron emissivity based on their MHD model. Mineshige et al. (2002) reported a preliminary examination, claiming that the radial density profile is significantly flatter than that of ADAF, leading to over-production of X-rays, but they calculated the spectra in a simplified way. Their results should be confirmed by full 3D radiative transfer calculations. More recently, Goldston, Quataert, and Igumenshchev (2005) calculated the spectra based on the simulated MHD flow by INA03, but only in the radio band. To our best knowledge nobody has yet calculated the emergent spectra in a wide range of wavelengths (from radio to X-ray). This prompted us to calculate, for the first time, the emergent spectra based on simulated 3D MHD flows by performing 3D Monte Carlo radiative transfer simulations and directly comparing them with the observed data of Sgr A*.

The plan of this paper is as follows: We present our model and the method of Monte Carlo radiative transfer in §2. The results will be displayed with the observational data in §3. We will demonstrate a serious discrepancy between them. A discussion of the loopholes, which cause the discrepancies, and how to remove them will be given in §4. The final section is devoted to conclusions.

2. MHD MODEL AND METHOD OF RADIATIVE TRANSFER CALCULATIONS

2.1. Overview of Adopted MHD simulations

Our spectral calculations are based on 3D MHD simulations by Kato, Mineshige, & Shibata (2004: hereafter referred to as KMS04). They investigated the evolution of a torus threaded by weak localized poloidal magnetic fields. The overall evolution of 3D MHD accretion flows is divided into two distinct phases (see Figure 1 in KMS04). In the first phase ($\tilde{t} \lesssim 1800$), toroidal magnetic fields are generated by differential rotation and are accumulated in the central region, driving a magnetic tower jet, where \tilde{t} is the time normalized by $r_s/c \sim 10^{-5}(M/M_\odot)s$ with M being the black-hole mass and r_s being the Schwarzschild radius. The jet is, however, a transient phenomenon. Eventually, ($\tilde{t} > 1800$), the jet ceases and a quasi-steady, geometrically thick density distribution with complex field configuration is produced.

In the quasi-steady state, the radial density profile is $\rho \propto r$ in the inner part ($r < 20r_s$), while $\rho \propto r^{-1}$ in the outer part ($r > 20r_s$) (see Figure 4 in KMS04). That is, there is a broad peak at $r \sim 20r_s$ in the density profile, which might be a remnant of the initial torus (discussed later). Note that this density profile differs from the results of some other 3D MHD simulations (see §4 for discussion). Also note that the density distribution of the ADAF model is significantly steeper; $\rho \propto r^{-a}$ with $a = 1 - 3/2$.

Throughout the present study, we set the black-hole mass to be $M = 2.6 \times 10^6 M_\odot$ (Schödel et al. 2002; Ghez et al. 2003). Thus, the normalized time corresponds to $t/\tilde{t} = 26$ s. We basically use the data of quasi-steady state at $\tilde{t} = 2210$ ($t = 5.7 \times 10^4$ s), when no obvious outflow is observed (see Figure 1 in KMS04), except at §3.3, where we will examine spectral variations.

2.2. Calculations of Physical Quantities

In the present study, we use Cartesian coordinates, (x, y, z) , where the black hole is located at the origin of the coordinate axes, the z -axis is set to be the rotation axis of the accretion flow, and the x - y plane corresponds to the equatorial plane. We employ Cartesian grids with numbers $(N_x, N_y, N_z) = (100, 100, 197)$ of cells. We assume that radiation is generated within the cylindrical region with radius, R ; $(x^2 + y^2)^{1/2} \leq R$ and $z \leq 100 r_s$. We consider the cases of $R = 10 r_s$ and $30 r_s$. The size of the calculating box is $2X \times 2Y \times 2Z$, where we set $(X, Y, Z) = (R, R, 100 r_s)$.

We take 3D data of density, magnetic fields, and proton temperature distributions in the accretion flows from the 3D MHD simulations (KMS04). Since the MHD simulation only give the normalized density, $\tilde{\rho}$, with the normalization, ρ_0 , and the normalized field strength, \tilde{B} , we have one free parameter, ρ_0 , to determine absolute values of density and magnetic fields; that is, $\rho = \rho_0 \tilde{\rho}$ and $B = (\rho_0 c^2)^{1/2} \tilde{B}$, where B is the field strength. The proton temperature does not depend on the density parameter and is given by the MHD simulation as $(\mu m_p c^2/k) \tilde{c}_s^2$, where μ is the mean molecular weight (=0.5), m_p is the proton mass, k is the Boltzmann constant, and \tilde{c}_s is the normalized sound velocity obtained by the simulation.

Although KMS04 assumed a one-temperature plasma, here we adopt two-temperature assumptions. Assuming that the electrons have a Maxwellian distribution, we evaluate the electron temperature, T_e , through the energy balance of the electrons between Coulomb collisions with ions and radiative cooling,

$$\int_{-Z}^Z \int_0^R \lambda_{ie} 2\pi r dr dz = \int L_\nu d\nu. \quad (1)$$

Here, λ_{ie} is the energy transfer rate from ions to electrons (Stepney & Guilbert 1983), L_ν is the luminosity at frequency, ν , respectively. In the present study, we suppose, for simplicity, the electron temperature to be a function of only the radius, r , and to be independent of the altitude, z . This simplification does not affect the results too much, since the emission from regions around the equatorial plane, where the density is at a maximum, is dominant at each radius. In addition, we solve for the electron temperature by dividing the calculating box into two parts; the inner ($r < 10r_s$) and outer parts ($r = 10 - 30 r_s$). The fractional luminosity, L_ν , is obtained by Monte Carlo simulations (see next subsection) for a given T_e , which does not always satisfy equation (1). We thus iteratively calculate the electron temperature and the emergent spectrum so as to meet the condition (1).

2.3. Monte Carlo Radiative Transfer Calculations

The method of the Monte Carlo simulation is based on Pozdnyakov, Sobol, & Sunyaev (1977). In this study, synchrotron emission/absorption, free-free emission/absorption, and Compton/inverse Compton scattering are taken into account. Some of the photons emitted by synchrotron and free-free emission pass through the calculating box without being scattered or absorbed, while some are scattered and/or absorbed in the accretion flow, depending on the mean free path at the photons emitting position. In order to efficiently calculate the emergent spectra, we introduce a weight, w , as described by Pozdnyakov, Sobol, & Sunyaev (1977). At the beginning, the weight, w_0 , is set equal to unity for each emitted photon and then we calculate the escape probability, P_0 . The escape probability of a photon after the i -th scattering (for $i \geq 1$), P_i , is evaluated as

$$P_i = \exp \left[- \left\{ \left(\frac{\rho(x_i, y_i, z_i)}{m_p} \right) \sigma_{KN}(x_i, y_i, z_i) + \kappa_\nu^{\text{abs}}(x_i, y_i, z_i) \right\} l \right], \quad (2)$$

where (x_0, y_0, z_0) corresponds to the point where a photon was generated, (x_i, y_i, z_i) is the point where a photon is subject to the i -th scattering, m_p is the proton mass, σ_{KN} is the Klein-Nishina cross section (Rybicki & Lightman 1979), κ_{abs} is the absorption coefficient, and l is the distance from the point (x_i, y_i, z_i) to the boundary of the calculating box, respectively. Assuming local thermodynamic equilibrium (LTE), we can write the absorption coefficient as

$$\kappa_\nu^{\text{abs}} = \frac{(\varepsilon_\nu^{\text{syn}} + \varepsilon_\nu^{\text{ff}})}{4\pi B_\nu}, \quad (3)$$

where $\varepsilon_\nu^{\text{syn}}$ and $\varepsilon_\nu^{\text{ff}}$ are the synchrotron and free-free emissivity, respectively (Pacholczyk 1970; Stepney & Guilbert 1983) and B_ν is the Planck function. The quantity

of $w_0 P_0$ represents the transmitted portion of photons and is recorded to calculate the penetrated spectrum or reprocessed photons according to the escape direction of the photon. A fraction of A_0 of the remaining portion, $w_1 \equiv w_0(1 - P_0)A_0$, undergoes at least one scattering, while $w_0(1 - P_0)(1 - A_0)$ describes the absorbed portion, where A_i ($i \geq 0$) is the scattering albedo. The transmitted portion of photons after the i -th scattering, $w_i P_i$, is recorded to calculate the transmitted spectrum, and the remaining portion, $w_i(1 - P_i)A_i$, undergoes the $(i+1)$ -th scattering. This calculation is continued until the weight w_i becomes sufficiently small ($w_i \ll 1$). The whole process is simulated by the Monte Carlo method. Finally, we suppose the region within the Schwarzschild radius, $(x^2 + y^2 + z^2)^{1/2} < r_s$, to be vacuum. Gravitational lensing as well as photon redshifts are not considered, since the black hole is much smaller than the calculating box in our study.

3. RESULTS: SPECTRAL FEATURES OF MHD FLOW

3.1. Basic features

We first display the representative spectra of the MHD flow in Figure 1 (see thick solid curves) together with the observed data of Sgr A*. The adopted parameters are the radius of the emitting region, $R = 30 r_s$, the elapsed time at $t = 5.7 \times 10^4$ s, and the density normalization, $\rho_0 = 1.6 \times 10^{-14} \text{ g cm}^{-3}$ (upper) and $5.6 \times 10^{-16} \text{ g cm}^{-3}$ (lower). It might be noted that the emission is predominantly from the equatorial plane and other parts at large altitudes ($|z| \gg 10 r_s$) do not contribute very much to the emergent spectra, although we sum up all the contri-

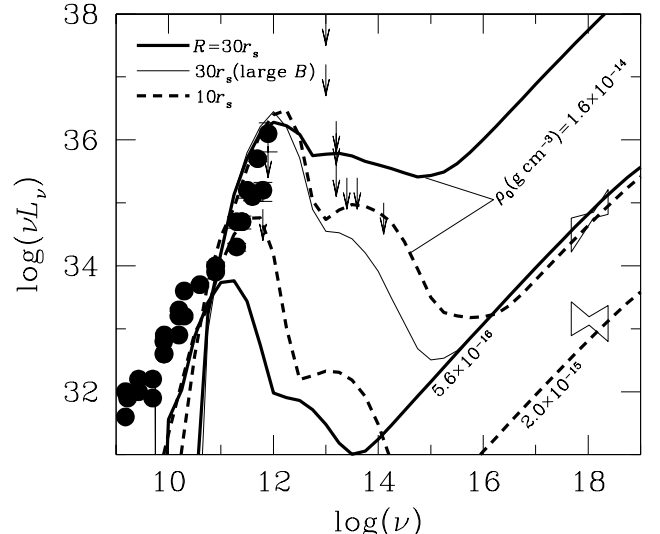


FIG. 1.— The emergent spectra of the MHD accretion flow and the observed data of Sgr A*. The thick solid curves are the resultant spectra for $R = 30 r_s$. Here, the adopted density parameters are $\rho_0 = 1.6 \times 10^{-14} \text{ g cm}^{-3}$ (upper) and $5.6 \times 10^{-16} \text{ g cm}^{-3}$ (lower), respectively. The thin solid curve indicates the spectrum, where the magnetic fields are set to be ten times stronger than the spectrum represented by the lower thick-solid curve. The spectra from the innermost part within $10 r_s$ are plotted by the dashed curves [$\rho_0 = 1.6 \times 10^{-14} \text{ g cm}^{-3}$ (upper dashed), $2.0 \times 10^{-15} \text{ g cm}^{-3}$ (lower dashed)]. The filled circles and the lines with arrows indicate the data and upper limits by radio and IR observations. For more detailed information regarding the data, please refer to Narayan et al. (1998). X-ray observations of the flaring and the quiescent state are shown by the two ‘bowties’ (Baganoff et al. 2001, 2003).

TABLE 1
CALCULATED ELECTRON TEMPERATURE.

ρ_0	$T_e(r \leq 10 r_s)$	$T_e(10 r_s < r < 30 r_s)$
$1.6 \times 10^{-14} \text{ g cm}^{-3}$	$5.56 \times 10^9 \text{ K}$	$3.45 \times 10^9 \text{ K}$
$5.6 \times 10^{-16} \text{ g cm}^{-3}$	$4.93 \times 10^9 \text{ K}$	$3.58 \times 10^9 \text{ K}$
$2.0 \times 10^{-15} \text{ g cm}^{-3}$	$5.20 \times 10^9 \text{ K}$	—
$3.0 \times 10^{-15} \text{ g cm}^{-3}$ (Our 2D)	$4.21 \times 10^9 \text{ K}$	$3.65 \times 10^9 \text{ K}$

Our 2D: our 2D MHD simulations

butions from the vertically elongated cylinder between $Z = \pm 100 r_s$. This is because the density rapidly decreases as $|z|$ increases. The calculated electron temperatures are listed in Table 1. As expected, electron temperatures are insensitive to radius, but there is a slight tendency that T_e decreases with an increase of radius. Similarly, relatively flat electron temperature profiles were obtained in two-temperature, hot accretion flows (Narayan & Yi 1995b; Nakamura et al. 1996; Manmoto, Mineshige, & Kusunose 1997) and evaporated disk-corona flows (Liu et al. 2002).

It is apparent that the resultant spectra look similar to those of the ADAF model. The lower-energy peak in the radio band is a synchrotron peak created because of significant self absorption of synchrotron emission. The IR emission at around $\log \nu = 14$ is due to inverse Compton scattering of synchrotron photons. Since we assume thermal electrons only, the spectral slope at $\log \nu < 11$ is $L_\nu \propto \nu^2$, corresponding to that of Rayleigh-Jeans emission. The electron temperatures do not vary much, even if we change ρ_0 , and, hence, the radio parts (which depends primarily on the electron temperature) are roughly identical among different models, as shown in Figure 1. In contrast, the flux at $\log \nu > 12$ and the frequency of the lower-energy peak (in the radio band) are both sensitive to ρ_0 .

Here, we stress that the magnetic field strength affects the lower-energy peak in the radio band and the IR flux, whereas the X-ray flux and the slope at $\log \nu < 11$ do not depend on the magnetic field strength itself. To check what alters if the magnetic field strengths were under or over-estimated in the simulation, we calculate the spectra with artificially strengthened magnetic fields, keeping the same density profile. The thin solid curve in Figure 1 indicates the spectrum, here the magnetic field strength is set to be ten times stronger than the original values, so as to be compared with the original (lower thick-solid curve). It is found that the X-ray flux and the slope at $\log \nu < 11$ do not change, but the radio peak luminosity and IR flux both increases. This is because the synchrotron emission contributes to the radio flux and inverse Compton scattering of the synchrotron photons is dominant in the IR band.

A big distinction between the spectra of ADAF and those of simulated MHD flows is found in the X-ray bands; namely, inverse Compton scattering is dominated in the former, while the thermal bremsstrahlung is the dominant mechanism in the latter. This reflects a flatter density profile in the MHD flow than for the ADAF, since a flatter density profile means that more material is present at large radii than the for case with a steep density profile, thereby producing more bremsstrahlung photons (discussed later).

We confirmed that the resultant spectra do not significantly change even if we employ the density and magnetic fields averaged over the azimuth in the simulated data of KMS04. This implies that 3D effects are not essential for the study of the spectra. This is because the flow pattern is almost axisymmetric in the simulations of KMS04, who calculated the evolution of a torus threaded by weak poloidal magnetic fields. In the case that the perturbations in the azimuthal direction increase, and non-axisymmetric structures form, any 3D aspects would clearly appear in the spectra.

3.2. Fitting to the flaring-state spectrum

A striking fact is that *we cannot fit both the radio and X-ray data simultaneously with the current MHD flow model*. The MHD flow model can reproduce only a part of the observations. For example, it can fit the observed radio peak, if we assign $\rho_0 = 1.6 \times 10^{-14} \text{ g cm}^{-3}$, but its flux largely exceeds the observed X-ray data and the upper limits in the IR band. This X-ray excess is caused by the strong free-free emission from the outer part of the flow ($r \gtrsim 10 r_s$), since the emissivity of free-free emission,

which is dominant in X-rays, is $\varepsilon^{\text{ff}} \propto \rho^2 T_e^{1/2} \propto r^{1.5}$ for a density profile of $\rho \propto r$ and the T_e profile of $T_e \propto r^{-1}$. The entire luminosity is $\varepsilon^{\text{ff}} d^3 r \propto r^{3.5} dr$.

For comparison, we plotted the spectra for the emission from only the inner region within $R = 10 r_s$ in Figure 1 (see the upper dashed curve) for the same density parameter, $\rho_0 = 1.6 \times 10^{-14} \text{ g cm}^{-3}$. The electron temperature is $5.56 \times 10^9 \text{ K}$ (see Table 1). As shown in this figure, huge X-ray excesses disappear (cf. the case with $R = 30 r_s$) and the model is successful in reproducing radio observations at around $\log \nu \sim 11 - 12$ and is consistent with X-ray observations during the flaring state (see the upper dashed curve).

The discrepancy between the upper thick-solid and upper dashed curves represents the contribution from the outer parts ($r > 10 r_s$). This clearly demonstrates that a huge X-ray excess is generated at the outer part of the flow and we need to somehow remove these contributions to fit the date.

Alternatively, we can reduce the X-ray flux so as to fit the data by employing a lower density parameter, $\rho_0 = 5.6 \times 10^{-16} \text{ g cm}^{-3}$ (see the lower thick-solid curve in Figure 1), but for such a case, radio peak flux decreases in accordance with the reduced density and, hence, is short of the radio luminosity. We thus see that for this particular density profile, it is totally impossible to reproduce the observations regardless of ρ_0 (see also Mineshige et al. 2002).

This situation resembles that of the CDAF (convection-dominated accretion flow; see Ball, Narayan, & QuataertBall 2001), since it has a flatter density profile like for the MHD flow (MM01). For $\rho \propto r^{-1/2}$ and $T \propto r^{-1}$, we have $\varepsilon^{\text{ff}} d^3 r \propto r^{0.5} dr$, indicating significant free-free emission from the outer parts.

Here, we stress that the emergent spectra starts to resemble to the observed data if the magnetic field strengths are systematically under-estimated in the 3D MHD simulation, that is, the actual magnetic fields are stronger than in the simulated data. As was already mentioned in the previous subsection, the radio peak luminosity and IR flux both increases with an increase of the

magnetic field strength. Therefore, the emergent spectra are consistent with the observations if the actual magnetic fields are ten times stronger than the simulated data (see the thin solid curve).

Strictly speaking, the calculated spectrum also deviates from the observed data at lower frequencies, $\log \nu < 10$. This inconsistency would be resolved if we consider synchrotron emission from nonthermal electrons as was first claimed by Mahadevan (1998). By a careful fitting to the up-to-dated spectrum, Yuan, Quataert, & Narayan (2003) concluded that the low-frequency radio flux can be explained via the emission of nonthermal electrons, which possess a small fraction of the electron thermal energy.

3.3. Case of the quiescent spectrum

What about the case of the quiescent spectrum? Before attempting any fitting to the quiescent spectrum, we need to remark on the observational constraints of the size of the emission region. By the Chandra X-ray observations, Baganoff et al. (2001, 2003) have claimed that the X-ray emission of Sgr A* is extended on scales of about 0.04 pc in the quiescent state. However, Tan & Draine (2004) suggested that about half of the extended X-ray emission is due to dust scattering from an unresolved source. Therefore, we regard the observed X-ray data in the quiescent state to give an upper limit for the X-ray luminosity of the accretion flow around the black hole.

To fit the X-ray flux in the quiescent state, we need to adopt a small density parameter, $\rho_0 = 2.0 \times 10^{-15} \text{ g cm}^{-3}$ (see the lower dashed curves), but, then, the flow can not reproduce a radio peak. In addition to this, the X-ray spectral slope also differs. The X-ray excess decreases with a decrease in size of the emission region, since the X-ray emission is dominated by the outer part, as we already mentioned in the previous subsection. We can adjust the X-ray luminosity to the observed value in the quiescent state by setting a much smaller emitting region, $R < 10 r_s$. However, the X-ray spectral slope is still much steeper than the observed one.

To summarize, we can reproduce the observed SED during the flaring state if the emitting region of the flow is restricted to be relatively small ($r < 10 r_s$), but cannot account for the quiescent-state spectrum for any choice of parameters. Note that a compact emission region is needed to account for short-term variability, since otherwise the variability timescale will be much longer in accordance with the timescales in the outer zone (Mineshige et al. 2002).

3.4. Time variation

MHD simulations show that MHD flows are highly time-variable. It is thus interesting to see how the resultant spectra change with time and check if the calculated trend fits the observational ones. We plot the time variations of the spectra in Figure 2. Here, we again set $R = 10 r_s$ and $\rho_0 = 1.6 \times 10^{-14} \text{ g cm}^{-3}$. The calculated epochs are divided into two phases; the jet phase ($t \lesssim 5 \times 10^4 \text{ s}$) and quasi-steady phase ($t \gtrsim 5 \times 10^4 \text{ s}$). The fluxes fluctuate in a wide range of frequencies as shown in the upper panel, although the electron temperature is kept nearly constant in the present study (see lower panel).

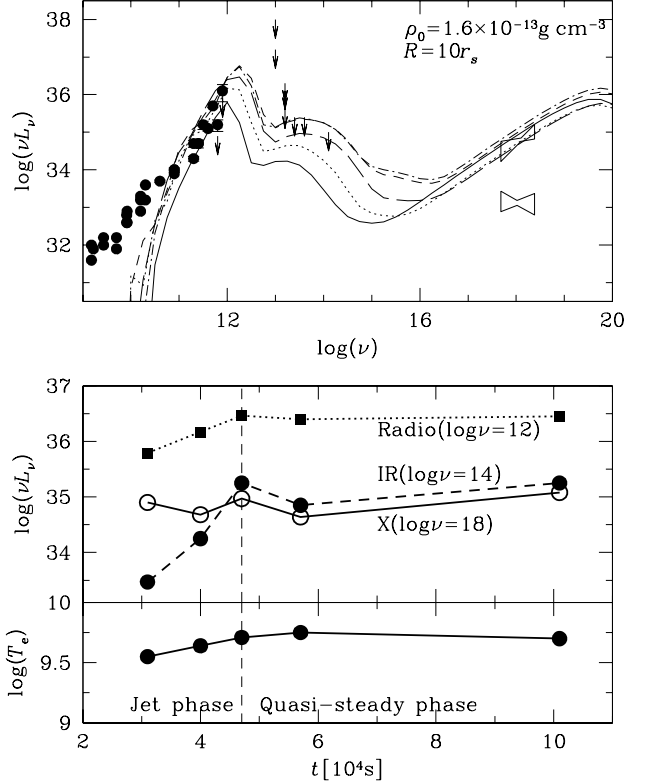


FIG. 2.— Spectral variations. Upper panel: the resultant spectra at $t = 3.1 \times 10^4 \text{ s}$ (solid), $t = 4.0 \times 10^4 \text{ s}$ (dotted), $t = 4.7 \times 10^4 \text{ s}$ (dashed), $t = 5.7 \times 10^4 \text{ s}$ (dot-dashed), and $t = 10.1 \times 10^4 \text{ s}$ (long-dashed), respectively. Here, we set $R = 10 r_s$ and $\rho_0 = 1.6 \times 10^{-14} \text{ g cm}^{-3}$. The lower panel: time variations of radio, IR, and X-ray luminosities as well as the electron temperature. The electron temperature is nearly constant. The radio and IR luminosities monotonously increase until the jet is produced ($t \lesssim 5 \times 10^4 \text{ s}$) while X-rays fluctuate. Radio luminosity is nearly constant at $t \gtrsim 5 \times 10^4 \text{ s}$, but the flux slightly fluctuates at IR and X-ray wavelengths and their amplitudes vary a few hundred percent.

As shown in this figure, the radio and IR luminosity increases until the jet is generated ($t \lesssim 5 \times 10^4 \text{ s}$), since magnetic fields are steadily being amplified in this phase. In the quasi-steady phase ($t \gtrsim 5 \times 10^4 \text{ s}$), in contrast, the radio luminosity is kept nearly constant, whereas IR and X-ray luminosities fluctuate and their variation amplitudes amount to a few hundred percent. These results are roughly consistent with the observed trends of multi-wavelength variability properties reported by Ulrich, Maraschi, & Urry (1997), who show that the largest amplitude variations are in the soft X-rays and that the optical-UV variation amplitude decreases systematically with increasing wavelength in the LLAGNs.

Interestingly, the calculated flux at each wavelength does not always vary coherently. We found that the X-ray luminosity decreases until $t \sim 4 \times 10^4 \text{ s}$, while the radio and IR luminosities increase. Moreover, only the radio luminosity does not vary so much between $t = 4.7 \times 10^4 \text{ s}$ and $t = 5.7 \times 10^4 \text{ s}$ in spite of the significant decrease in the IR and X-ray luminosities (see lower panel). A comparison of such trends with the observations is left for future work.

The X-ray time-variation predicted by our results is too small to account for the observed large-amplitude variations (X-ray burst) reported by Baganoff et al. (2003), i.e., the X-ray luminosity in the flaring state is about 45

times larger than that in the quiescent state. Such an X-ray flaring event might be produced by the nonthermal electrons, whereas we take only thermal electrons into account in the present study.

4. DISCUSSION: THE IMPLICATIONS OF OUR RESULTS

We have calculated the emergent spectra based on the MHD simulation by KMS04 and demonstrated that the MHD flow model cannot account for both of the radio and X-ray observations in the flaring state simultaneously, unless we restrict the emission region to be compact. We have also shown that it is problematic for reproducing the spectrum in the quiescent state. In this section, we discuss what these results imply.

4.1. flaring state

We first focus our discussion on the case of the flaring state. As was already mentioned in §3.2, the relatively compact emission region ($r < 10 r_s$) is required for the MHD flow model to reproduce the observed spectrum in the flaring state of Sgr A*. There are several possibilities which meet this requirement.

4.1.1. Modifying density profiles

A compact emission region would be realized, if the density profile at large radii would be much steeper than that obtained by KMS04 or if the broad density peak found in KMS04 is somehow removed. Since KMS04 provides only one specific example, it is necessary to check the density profiles of other MHD simulations. In Table 2 we summarize the density profiles of some representative simulations with brief descriptions of their calculations.

SP01, HB02, and KMS04 adopted similar initial conditions; namely, they started calculations with a torus threaded by weak localized poloidal magnetic fields and assumed no further mass input. They all investigated the evolution of the torus under the pseudo-Newtonian potential. INA03 and Proga & Begelman (2003: hereafter referred to as PB03) set a different situation; INA03 continuously injected magnetized matter into the computational domain from near the outer boundary, and PB03 started the simulations with Bondi accretion flow, whose angular momentum is zero except for the outer part of

the flow. Note that SP01 and PB03 performed 2D simulations, while others did 3D simulations. Despite some differences in simulations, both of SP01, INA03, and PB03 obtained a relatively steep density profile, $\rho \propto r^{-1}$. No obvious density peak is found in their simulations.

HB02 obtained a similar density profile but with a remarkable peak at $\sim 5 r_s$, which may be a remnant of the initial torus. Caution should be taken here, since this peak may be transient. Similarly, the density peak found at $\sim 20 r_s$ in KMS04, which mainly contributes to X-ray emissions, might be a direct consequence of the initial torus located at $40 r_s$ at the beginning of the simulations. If this density peak is removed by long term numerical calculations, we expect that the large X-ray excess may disappear and the resultant spectra can be consistent with the observations, even if we do not artificially restrict the emission region.

To see if this is the case, we made the following test. We performed 2D MHD simulations, starting from the similar initial condition to that of KMS04 but with the initial torus being put a much larger radius, around $\sim 100 r_s$. After a long time interval, we have confirmed that the broad density peak, a remnant of the initial torus, disappears. The resultant density structure in this 2D model (at $\tilde{t} = 8200$) is plotted by the solid curve in the upper panel in Figure 3 with that of KMS04. The density profile of our 2D model is roughly proportional to r^{-1} at $r > 7 r_s$ and roughly agrees with the simulations by SP01, INA03 and PB03.

We next, calculate the spectrum based on our 2D model and plot it in Figure 3 (lower panel). The adopted density parameter is $\rho_0 = 3.0 \times 10^{-15} \text{ g cm}^{-3}$, and the size of the emitting region is $R = 30 r_s$. The calculated electron temperature is shown in Table 1. Clearly, our 2D MHD model can nicely fit the observed data points during the flaring state. Thus, it is very likely that if we continue MHD simulations from the data by KMS04 further, we may be able to fit the observational data. We need caution, however, because behavior of the magnetic fields in 2D and 3D simulations may be distinct. We cannot trust the 2D data so much. We need to perform longer 3D simulations to confirm our tentative conclusions.

It is expected that the MHD models by INA03, SP01, and PB03 can also reproduce the observed SED during the flaring state, since these models have similar density profiles to those of our 2D model (see the upper panel of Figure 3). We demonstrate it by calculating the spectrum from the regions at $r < 30 r_s$ of the spherical flow model, which is constructed based on the 3D MHD simulations of INA03 (see the dotted curve in the lower panel of Figure 3). In this model the density and proton temperature profiles are set to be $\rho = 7.0 \times 10^{-15} (r/r_s)^{-1} \text{ g cm}^{-3}$ and $T_p = 8.6 \times 10^{11} (r/r_s)^{-1} \text{ K}$, respectively. The electron temperature and the plasma- β are assumed to be constant in the calculating box, $T_e = 5 \times 10^9 \text{ K}$ and $\beta = 3$. The INA03 model shows a similar SED with that of our 2D model, and is consistent with the observed data in the flaring state. The other MHD models by HB02, MMM01, and MM03, on the other hand, have flatter density profiles, $\rho \propto r^{-a}$ with $a = 0 - 1/2$ (see Table 2). Hence, they will produce an X-ray excess as was in the case of our simulation.

TABLE 2
LIST OF MHD MODELS

ref.	Ψ	I.C./B.C.	jet	ρ -profile	ρ -peak
SP01	PN	B_p -torus	yes	$r^{0.1} (< 10 r_s), r^{-1} (> 10 r_s)$	$10 r_s$
MMM01	N	B_ϕ -torus	no	$r^{-1/2}$	—
HB02	PN	B_p -torus	yes	$r^0 + \text{torus} (r < 10 r_s)$	$5 r_s$
INA03	PN	injection	yes	$r^{-1/2} (< 10 r_s), r^{-1} (> 10 r_s)$	$3 r_s$
MM03	PN	B_ϕ -torus	no	r^0	$3 r_s$
PB03	PN	Bondi flow	yes	$r^{0.2} (< 7 r_s), r^{-1} (> 7 r_s)$	$7 r_s$
KMS04	PN	B_p -torus	yes	$r^1 (< 20 r_s), r^{-1} (> 20 r_s)$	$20 r_s$
Our 2D	PN	B_p -torus	yes	$r^1 (< 7 r_s), r^{-1} (> 7 r_s)$	$7 r_s$

SP01: Stone & Pringle (2001); MMM01: Machida, Matsumoto & Mineshige (2001); HB02: Hawley & Balbus (2002); INA03: Igumenshchev, Narayan, & Abramowicz (2003); MM03: Machida & Matsumoto (2003); Our 2D: our 2D MHD simulations; Ψ : gravitational potential; N: Newtonian; PN: pseudo-Newtonian; I.C./B.C.: initial or boundary condition; B_ϕ - or B_p -torus: A torus threaded by weak localized toroidal or poloidal magnetic fields is initially assumed.; injection: Magnetized matter is continuously injected into the computational domain near the outer boundary

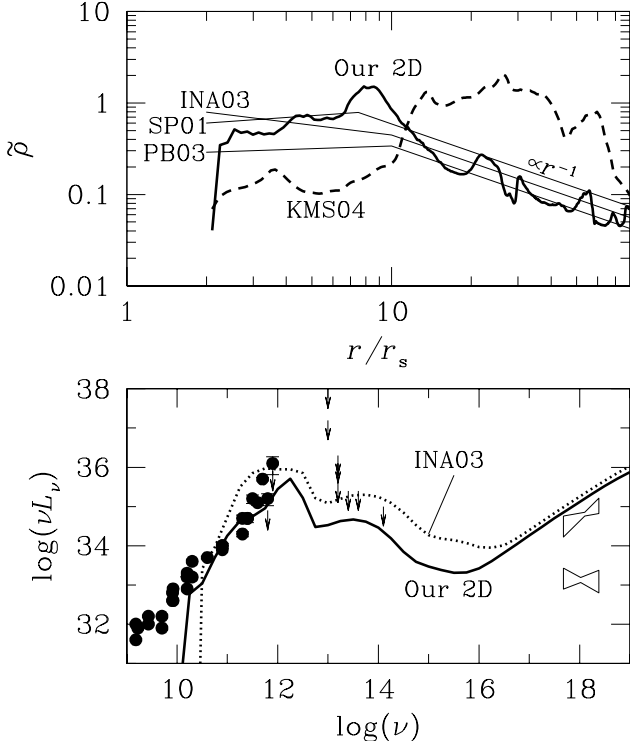


FIG. 3.— Upper panel: The normalized density profile given by our 2D MHD simulations (thick solid) and KMS04 (dashed). The density peak in KMS04 is around $20 r_s$, in contrast, it is near the black hole ($r \sim 7 r_s$) in the case of our 2D simulations. The thin solid curves indicate the schematic density profile given by INA03 (3D simulations), SP01, and PB03 (2D simulations). They showed a similar density profile, $\rho \propto r^{-1}$, with our 2D MHD simulations at the outer part ($r > 10 r_s$). Lower panel: The solid curve is the spectra of our 2D MHD model. We consider the emission from the extended region of $r < 30 r_s$. The normalization of density is set to be $\rho_0 = 3.0 \times 10^{-15} \text{ g cm}^{-3}$, and the calculated electron temperature is shown in Table 1. The dotted curve represents the spectra of the INA03 model. Here, we use the spherical flow model, which is constructed based on the 3D MHD simulations of INA03. In this model, the density and proton temperature profiles are $\rho = 7.0 \times 10^{-15} (r/r_s)^{-1} \text{ g cm}^{-3}$ and $T_p = 8.6 \times 10^{11} (r/r_s)^{-1} \text{ K}$, respectively. We set $T_e = 5 \times 10^9 \text{ K}$ and plasma- $\beta = 3.0$. Our 2D MHD model as well as the INA03 model can reproduce the observed data during the flaring state.

4.1.2. Moderate radiative cooling

A distinct way of possibly producing a steeper density profile is to introduce moderate radiative cooling (Mineshige et al. 2002). By the terminology of RIAF it means that radiative loss is inefficient. However, it may happen that radiative cooling is only partly and transiently important. If we set the cooling timescale to be comparable to the accretion timescale, we expect that only dense parts can efficiently be cooled. Since the density is generally higher in the innermost region, cooling results in further mass concentration towards the center, a preferable condition to fit the observations. However, this is only a possibility and we need 3D MHD simulations to confirm this idea.

Another possibility is that the outer portions of the disk may become radiation efficient flow. Even if the density profile does not change, the emission from the outer parts can be reduced, if the electron temperature there were much lower than that of the inner part. In KMS04 and most of other MHD simulations, the one-temperature plasma is assumed and the cooling of pro-

tons is neglected. However, the proton thermal energy may be converted into the electron energy due to the effective Coulomb collisions and be radiated away in the outer zones. Further study requires 3D MHD simulations coupled with the electron energy equation and radiative cooling.

4.2. Quiescent state

The case of the quiescent spectrum will be much more difficult to reproduce by the MHD model. We have seen that the calculated spectral slope was much steeper than that of the X-ray observations in the quiescent state of Sgr A*. We can reduce the X-ray flux but cannot easily change the spectral slope in the X-ray range. We find two possibilities to make a flatter spectral slope.

4.2.1. Nonthermal electrons

This difficulty may be removed, if emission from the nonthermal electrons dominates over that from thermal ones. By considering emission from nonthermal electrons, Yuan, Quataert, & Narayan (2003) nicely reproduced the observed spectrum in the quiescent state of Sgr A*. [However, they prescribe an arbitrary energy distribution of the nonthermal electrons with more free parameters in order to give a good fit to the observations.] This is a very attractive possibility, but it is hard to prescribe an energy distribution of nonthermal electrons because of a lack of good theory of particle acceleration. Thus we need to introduce parameters describing the electron energy distribution and the results strongly depend on these parameters.

4.2.2. Compton scattering in disk coronae

The spectral slope at the X-ray band would be flatter if inverse Compton scattering is more enhanced, compared with other processes, and becomes dominant in the X-ray range. Note that the calculated steep spectral slopes shown in Figure 1 are due to bremsstrahlung emissions from the outer parts. The relative importance of the Comptonization inside the corona is proportional to the column density, $\sim \rho H$ (with H being the half-thickness of the corona), while the bremsstrahlung emissivity is proportional to $\rho^2 H$. Thus, the presence of an extended, tenuous corona may resolve the problem. However, the formation mechanism of the corona is still an open issue and it is not easy to probe this possibility.

5. CONCLUSIONS

In order to test the 3D MHD flow simulation as a model of optically-thin, high-temperature accretion flows through comparison with observations, we studied the spectral properties of magnetized accretion flows based on the 3D MHD simulation data. Surprisingly, such comparative studies have not been well investigated so far in spite of a large number of MHD simulations having been performed recently. We summarize our results as followings:

1. We found that the MHD model cannot reproduce the observed SED in the flaring state of Sgr A* without substantial modification. If we use the data by KMS04, we need to require that the emission region is restricted to be compact ($r < 10 r_s$),

but this could be due to the particular initial condition. Some other MHD models with a steeper density profile ($\rho \propto r^{-1}$) and without a broad density peak ($r > 10r_s$) can fit the observations, if the emissions from regions of $r \lesssim 30r_s$ mainly contributes to the SEDs.

2. The MHD flow can not generally reproduce the spectrum (spectral shape, in particular) in the quiescent state. Significant contributions by nonthermal electrons should resolve this issue. It is also possible that observational X-ray data may contain emissions from regions other than the vicinity of the black hole.
3. The MHD flow predicts substantial and incoherent time variations in the emergent spectrum. The pre-

dicted variation amplitude is, however, too small to account for the large-amplitude X-ray burst.

The authors would like to thank the anonymous referee for important comments and suggestions. The calculations were carried out at Yukawa Institute for Theoretical Physics at Kyoto University and the Department of Physics at Rikkyo University. This work is supported in part by Research Fellowship of the Japan Society for the Promotion of Science for Young Scientists, 02796 (KO) and the Grants-in-Aid of the Ministry of Education, Science, Culture, and Sport, (14079205, 16340057) and by a Grant-in-Aid for the 21st Century COE “Center for Diversity and Universality in Physics” (SM).

REFERENCES

Abramowicz, M. A., Chen, X., Kato, S., Lasota, J.-P., & Regev, O. 1995, ApJ, 438, L37

Baganoff, F. K., et al. 2001, Nature, 413, 45

Baganoff, F. K., et al. 2003, ApJ, 591, 891

Balbus, S. A. 2003, ARA&A, 41, 555

Ball, G. H., Narayan, R., & Quataert, E. 2001, ApJ, 552, 221

Ebisawa, K. 1999, in High Energy Processes in Accreting Black Holes (ASP Conf. Ser. 161), ed. J. Poutanen & R. Svensson, p.39

Esin, A., McClintock, J. E., & Narayan, R. 1997, ApJ, 189, 865

Ghez, A. M. et al. 2003, ApJ, 586, L127

Goldston, J. E., Quataert, E., & Igumenshchev, I. V. 2005, ApJ in press (astro-ph/0411627)

Hawley, J. F. 2000, ApJ, 528, 462

Hawley, J. F. 2001, ApJ, 554, 534

Hawley, J. F. & Balbus, S. A. 2002, ApJ, 573, 738

Hawley, J. F., Balbus, S. A. & Stone, J. M. 2001, ApJ, 554, L49

Hawley, J. F. & Krolik, J. H. 2001, ApJ, 548, 348

Ichimaru, S. 1977, ApJ, 214, 840

Igumenshchev, I. V. & Abramowicz, M. A. 2000, ApJS, 130, 463

Igumenshchev, I. V., Narayan, R., & Abramowicz, M. A. 2003, ApJ, 592, 1042

Kato, S., Fukue, J., & Mineshige, S. 1998, Black-Hole Accretion Disks (Kyoto: Kyoto Univ. Press)

Kato, Y., Mineshige, S., & Shibata, K. 2004, ApJ, 605, 307 (KMS04)

Kawaguchi, T., Mineshige, S., Machida, M., Matsumoto, R., & Shibata, K. 2000, PASJ, 52, L1

Liu, B. F., Mineshige, S., Meyer, F., Meyer-Hofmeister, E., & Kawaguchi, T. 2002, ApJ, 575

Machida, M., Hayashi, M. R., & Matsumoto, R. 2000, ApJ, 532, L67

Machida, M. & Matsumoto, R. 2003, ApJ, 585, 429

Machida, M., Matsumoto, R., & Mineshige, S. 2001, PASJ, 53, L1

Mahadevan, R. 1998, Nature, 394, 651

Malkan, M. A. 1983, ApJ, 268, 582

Manmoto, T. 2000, ApJ, 534, 734

Manmoto, T., Mineshige, S., & Kusunose, M. 1997, ApJ, 489, 791

Matsumoto, R. 1999, in Numerical Astrophysics, ed. S. M. Miyama, K. Tomisaka, & T. Hanawa (Boston: Kluwer Academic), p.195

Mineshige, S., Hirano, A., Kitamoto, S., Yamada, T.T., & Fukue, J. 1994, ApJ, 426, 308

Mineshige, S., & Makishima, K. 2004, PThPS, Stellar-Mass, Intermediate-Mass, and Supermassive Black Holes, in press

Mineshige, S., Negoro, H., Matsumoto, R., Machida, M., & Manmoto, T. 2002, in Current High-Energy Emission around Black Holes, ed. Lee, C.-H. & Chang, H.-Y. (Singapore: World Scientific), 119

Mitsuda, K. et al. 1984, PASJ, 36, 741

Nakamura, K. E., Matsumoto, R., Kusunose, M., & Kato, S. 1996, PASJ, 48, 761

Narayan, R. 2002, in Lighthouses of the Universe, ed. M. Gilfanov, R. Sunyaev, & E. Churazov (Berlin: Springer), 405

Narayan, R., Mahadevan, R., & Quataert, E. 1998, in The Theory of Black Hole Accretion Discs, ed. M. A. Abramowicz, G. Björnsson, & J. E. Pringle (Cambridge: Cambridge Univ. Press), 148

Narayan, R., Mahadevan, R., Grindlay, J. E., Popham, R. G., & Gammie, C. 1998, ApJ, 492, 554

Narayan, R. & Yi, I. 1994, ApJ, 428, L13

Narayan, R. & Yi, I. 1995a, ApJ, 444, 231

Narayan, R. & Yi, I. 1995b, ApJ, 452, 710

Narayan, R., Yi, I., & Mahadevan, R. 1995, Nature, 374, 623

Oka, K. & Manmoto, T. 2003, MNRAS, 340, 543

Özel, F., Psaltis, D., & Narayan, R. 2000, ApJ, 541, 234

Pacholczyk, A. G. 1970, Radio Astrophysics (San Francisco: Freeman)

Pozdnyakov, L. A., Sobol, I. M., & Sunyaev, R. A. 1977, Soviet Astron., 21, 708

Rybicki, G. B. & Lightman, A. P. 1979, Radiative Processes in Astrophysics (New York: John Wiley & Sons, Inc.)

Schödel, R., et al. 2002, Nature, 419, 694

Shakura, N. I. & Sunyaev, R. A. 1973, A&A, 24, 337

Shields, G. A. 1978, Nature, 272, 706

Stepney, S. & Guilbert, P. W. 1983, MNRAS, 204, 1269

Stone, J. M. & Pringle, J. E. 2001, MNRAS, 322, 461

Tan, J. C. & Draine, B. T. 2004, ApJ, 606, 296

Ulrich, M.-H., Maraschi, L., & Urry, C. M. 1997, ARA&A, 35, 445

Yuan, F., Quataert, E., & Narayan, R. 2003, ApJ, 598, 301